

Revised Magnetic Structure and Tricritical Behavior of the CMR Compound NaCr_2O_4 Investigated with High Resolution Neutron Diffraction and μ^+ SR

E. Nocerino^{1,*}, O. K. Forslund², H. Sakurai³, A. Hoshikawa⁴, N. Matsubara¹, D. Andreica⁵, A. Zubayer⁶, F. Mazza⁷, J.-C. Orain⁸, T. Saito⁹, J. Sugiyama^{10,11}, I. Umegaki¹², Y. Sassa², and M. Månsson^{1,†}

¹KTH Royal Institute of Technology, Department of Applied Physics, Alba Nova University Center, Stockholm, SE-114 21, Sweden

²Chalmers University of Technology, Department of Physics, Göteborg, SE-412 96, Sweden

³National Institute for Materials Science, Namiki, Tsukuba, Ibaraki 305-0044, Japan

⁴Frontier Research Center for Applied Atomic Sciences, Ibaraki University, 162-1 Shirakata, Tokai, Ibaraki 319-1106, Japan

⁵Faculty of Physics, Babes-Bolyai University, 3400 Cluj-Napoca, Romania

⁶Department of Physics, Chemistry and Biology (IFM), Linköping University, SE-581 83 Linköping, Sweden

⁷Institute of Solid State Physics, TU Wien, Wiedner Hauptstraße 8-10, AT-1040 Wien (Austria)

⁸Laboratory for Muon Spin Spectroscopy, Paul Scherrer Institute, CH-5232, Villigen, PSI, Switzerland

⁹Institute of Materials Structure Science, High Energy Accelerator Research Organization, 203-1 Shirakata, Tokai, Ibaraki 319-1107, Japan

¹⁰Neutron Science and Technology Center, Comprehensive Research Organization for Science and Society (CROSS), Tokai, Ibaraki 319-1106, Japan

¹¹Advanced Science Research Center, Japan Atomic Energy Agency, Tokai, Ibaraki 319-1195, Japan

¹²Muon Science Laboratory, Institute of Materials Structure Science, KEK, Tokai, Ibaraki 319-1106, Japan

ABSTRACT

The mixed valence Cr compound NaCr_2O_4 , synthesized using a high-pressure technique, offers a unique playground for investigating unconventional physical properties in condensed matter. In the present study, muon spin rotation/relaxation (μ^+ SR) and high-resolution neutron powder diffraction (NPD) measurements were carried out to clarify the true magnetic ground state of this interesting compound. Our detailed study brings new insight, allowing us to confirm the existence of a commensurate antiferromagnetic order (C-AFM) and to extract its ordered Cr moment $\mu_{\text{Cr}}^{\text{C}} = (4.30 \pm 0.01)\mu_B$. Such a value of the ordered moment is in fact compatible with the existence of high-spin Cr sites. Further, the value of the canting angle of the Cr spin axial vector is refined as $\theta_c = (8.8 \pm 0.5)^\circ$. Employing high-quality samples in combination with time-of-flight NPD, a novel magnetic supercell was also revealed. Such supercell display an incommensurate (IC)-AFM propagation vector $(0\ 0\ \frac{1}{2} - \delta)$, having an ordered moment $\mu_{\text{Cr}}^{\text{IC}} = (2.20 \pm 0.03)\mu_B$. It is suggested that the C-AFM and IC-AFM modulations are due to itinerant and localized contributions to the magnetic moment, respectively. Finally, the direct measurement of the magnetic order parameter provided a value of the critical exponent $\beta = 0.245 \approx \frac{1}{4}$, suggesting a non conventional critical behavior for the magnetic phase transition in NaCr_2O_4 .

Introduction

Mixed valence transition metal oxides constitute a very attractive scientific playground as they offer a vast range of diverse physical properties, such as unconventional superconductivity, metal-insulator transitions, colossal magneto-resistance and exotic magnetic ground states¹⁻⁷. Among them, mixed valence state Cr oxides are rather rare because of the intrinsic stability of Cr^{3+} ions in octahedral coordination with O atoms. Here the half-filled t_{2g} states of the $3d^3$ Cr^{3+} orbitals tend to not coexist with Cr^{4+} ions, which would instead form a less-than-half filled $3d^2$ state. Due to the plethora of its unusual physical properties, a lively interest surrounds the compound NaCr_2O_4 . Here, Cr has formal valence $\text{Cr}^{3.5+}$, given by the mix in equal parts of Cr^{3+} and Cr^{4+} valence states⁸, which can only be achieved thanks to the high pressure synthesis technique employed to stabilize this material⁹. The high pressure indeed forces a complex crystal-field symmetry and orbital ordering for the Cr ions in NaCr_2O_4 ¹⁰, which crystallizes in a calcium ferrite-type structure with space group $Pnma$. here, the Cr atoms occupy the two distinct

crystallographic positions Cr1 and Cr2, octahedrally coordinated by O atoms (Fig. 1). The CrO_6 octahedra associated to the two sites are tilted with respect to the each other and distorted, with $\text{O}-\text{Cr}-\text{O} \neq 90^\circ$ angles and Cr-O distances that are equal to each other on one side of the octahedron and different of the other side [Fig. 1(a)], leading to four crystallographically different oxygen sites. The edge sharing connections between the equal Cr-O sides of the octahedra, form zig-zag Cr chains along the b -axis, via the Cr1-O2-Cr1 and the Cr2-O4-Cr2 bonds. The corner sharing connections between the non-equal Cr-O sides, instead, form rutile slabs in the ac -plane via the Cr1-O1-Cr2 (along a) and the Cr1-O3-Cr2 (along c) bonds [Fig. 1(a,b)].

The difference between the two Cr sites lays in their orbital structure, since different distortions in the CrO_6 octahedra lift the degeneracy on the Cr $3d$ orbitals in different ways. In particular, following the labelling of the current work, for Cr1 the d_{xy} orbital is almost fully occupied with a localized nature, while the $d_{yz\pm xz}$ have an itinerant nature. Vice versa, for Cr2 the d_{xy} and $d_{yz\pm xz}$ are almost fully occupied while the d_{yz-xz} has an itinerant nature¹⁰. Such a combination of orbital filling leads to a dual itinerant-localized character for the Cr electrons. Such CrO_6 network, designs honeycomb-like distorted hexagonal one-dimensional channels (along b -axis), in which the Na^+ ions are located [Fig. 1(a)].

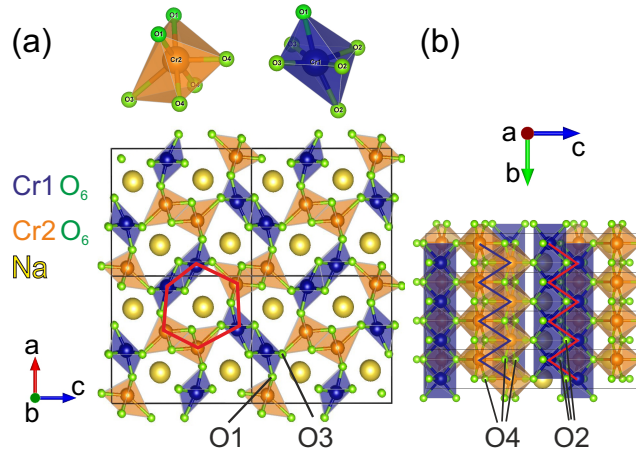


Figure 1. Crystal structure of NaCr_2O_4 . (a) ac -plane orientation of the unit cell; the hexagonal channel that hosts the Na^+ ions is highlighted in red. A detailed picture of the distorted octahedra for both Cr1 and Cr2 sites are also shown. The crystallographic sites for the O atoms are explicitly displayed to evidence the uneven distribution of the Cr-O distances. (b) bc -plane orientation of the unit cell; the zig-zag chains along the b -axis are highlighted by the solid lines.

NaCr_2O_4 exhibits an antiferromagnetic (AFM) transition $T_N = 125$ K and, below this temperature, it manifests colossal magneto-resistance (CMR)¹¹ as well. This is already surprising in itself since CMR is usually a physical property related to manganites¹² but, in addition, the CMR of NaCr_2O_4 is also anomalous. In conventional CMR systems, the presence of an applied magnetic field causes a dramatic reduction of the electrical resistivity in a limited temperature interval around a ferromagnetic transition. This effect causes hysteresis in the magnetic and transport measurements, and the system is still metallic even in absence of magnetic field. Under zero magnetic field, NaCr_2O_4 behaves as an insulator with its electrical resistivity diverging while cooling. In the presence of an applied magnetic field, the resistivity is dramatically reduced (i.e. the CMR effect), but this effect is not limited to the region of temperatures around the AFM transition. On the contrary, it is more and more enhanced as the temperature is lowered, without any thermal or field hysteresis. The mechanism underlying conventional CMR in manganites is explained as a magnetic field-induced suppression of the thermal fluctuation of the parallel moments, causing the CMR to disappear at temperatures below the FM transition¹³. Since the CMR in NaCr_2O_4 shows a behavior that is the exact opposite of the conventional case, the underlying mechanism must be entirely new.

Beyond the anomalous CMR, NaCr_2O_4 was also found to exhibit an unusual coexistence of positive and negative charge transfer states (via XAS measurements⁸). Here, the charge frustration induced by the highly degenerate charge ordering configurations of the $\text{Cr}^{4+} 3d^2$ electronic state, is removed by establishing a $3d^3 \bar{L}$ state (as suggested by ^{53}Cr -NMR measurements¹⁴), in which Cr ions share a hole through the ligand oxygen. Calculations of the electronic structure showed that such holes are unevenly distributed and are found preferentially at the corner sharing oxygen sites O1 and O3¹⁰ (fig. 1(a)).

Concerning the magnetic properties of NaCr_2O_4 , magnetic susceptibility measurements displayed a large positive value for the Curie-Weiss temperature, indicative of dominant ferromagnetic (FM) interactions. However, the AFM character of the susceptibility (showing the typical AFM cusp), suggested non negligible AFM interactions⁹. Remarkably, a dramatic increase in the magnetization with the application of a relatively small external field of 3.5 T was also observed in bulk magnetic measurements⁹. This behavior was interpreted as a spin-flop transition. Since the Cr zig-zag chains form triangular Cr lattices,

it was suggested that a competition between FM and AFM exchange interactions are present within the chains. This would lead to spin frustration (consistent with the supposed spin-flop transition) and a complex magnetic ordering in NaCr_2O_4 , similar to the isostructural compounds NaV_2O_4 and CaCr_2O_4 ^{7,15}). The fact that the negative CMR in this material only appears below T_N , suggests that this effect should be closely related to the magnetic structure. Therefore, spin frustration was regarded as a main responsible for the presence of unconventional CMR in NaCr_2O_4 .

Earlier magnetic measurements using muon spin rotation/relaxation (μ^+ SR) and neutron powder diffraction (NPD) methods of the NaCr_2O_4 compound have actually been published^{16–18}. Such studies revealed the occurrence of a commensurate canted antiferromagnetic (C-AFM) order with a Néel temperature $T_N = 125$ K. A spin structure was presented with the Cr moments aligned ferromagnetically along the b -axis in each chain, and antiferromagnetically in the ac -plane among adjacent chains, with propagation vector $k = (1\ 0\ 1)^{16}$. However, the value of the canting angle could not be precisely estimated. In this work we revisit this interesting compound using high-quality samples studied by state-of-the-art μ^+ SR and high resolution NPD techniques. We present a detailed and thorough study of the temperature dependent magnetic properties in NaCr_2O_4 that shed new light on the underlying physics and reveal a series of completely novel properties that were previously overlooked or misinterpreted¹. Among other things, the canting angle of the Cr spin axial vector and its magnitude was clarified in detail. Moreover, an additional incommensurate (IC) modulation of the magnetic structure was observed. A slightly revised mechanism underlying the magnetic ordering was proposed and indications of a tricritical behavior as well as, possibly, metamagnetism emerged from the temperature dependence of the magnetic order parameter. Our results are consistent with the presence of high- and low-spin Cr sites in the magnetic ground state of NaCr_2O_4 . Such Cr spin states are also foreseen by a recently published theoretical investigation, according to which a spin disproportionation exists between the Cr1 and Cr2 sites in NaCr_2O_4 ²⁰. The intra-chain FM alignment of the Cr moments along the b -axis, and a weak coupling between the magnetic ordering and the crystal structure, suggest that no spin frustration is in place along the zigzag chains. In fact, in other Q1D calcium-ferrite type compounds the magnetic order develops along the geometrically frustrated Cr zigzag ladders (e.g., β - CaCr_2O_4 and NaMn_2O_4 ^{6,15}). However, the magnetic interactions in NaCr_2O_4 instead "escape" the Q1D Cr chains and realize a 2D magnetic structure, developing across the double rutile strings in the ac -plane. This observation is also consistent with electronic structure calculations¹⁰, which suggest that such kind of 2D magnetic structure is a very likely ground state. The absence of geometrical frustration, and the indications of tricritical behavior of the magnetic order parameter, suggest that the spin flop transition observed as a function of external magnetic field⁹ could instead be interpreted as metamagnetism.

Results

In the following section the experimental results with the related data analysis are collected. In the first subsection the temperature dependent μ^+ SR measurements are presented, while the second subsection shows the NPD measurements for different temperatures.

μ^+ SR Results

In the wTF μ^+ SR measurements an external magnetic field is applied orthogonal to the initial spin-polarization of the muon beam, causing it to precess around the external field's direction. In this configuration, μ^+ SR time spectra have been acquired in the temperature range $T = 2 - 145$ K. The applied field wTF = 50G, is several orders of magnitude smaller than the internal field at the muon sites. Selected wTF spectra acquired for the NaCr_2O_4 are shown in Fig. 2(a). At high temperature the magnetic moments in the sample are randomly oriented, therefore the local internal magnetic field is negligible with respect to the external field, which causes the muon spins to precess accordingly. Indeed the spectrum at $T = 145$ K exhibits a very regular oscillation, with a single frequency related to the wTF. As the temperature decreases, the system gradually goes from the paramagnetic (PM) to the AFM phase. The strong internal AFM field overcomes the weak external field, the overall depolarization rate increases and the amplitude of the wTF oscillation in the spectra are reduced, until only the high frequency oscillations in the early time domain are left [Fig. 2(a)]. The fit function chosen for the wTF spectra is the following:

$$A_0 P_{\text{TF}}(t) = A_{\text{TF}} \cos(2\pi\nu_{\text{TF}}t + \frac{\pi\phi}{180}) \cdot e^{(-\lambda_{\text{TF}}t)} + A_{\text{AFM}} \cos(2\pi\nu_{\text{AFM}}t + \frac{\pi\phi}{180}) \cdot e^{(-\lambda_{\text{AFM}}t)} + A_{\text{tail}} \cdot e^{(-\lambda_{\text{tail}}t)}. \quad (1)$$

Here A_0 is the initial asymmetry, $P_{\text{TF}}(t)$ is the muon spin polarization function, A_{TF} , A_{AFM} and A_{tail} are the asymmetries of the related polarization components, $\nu_{\text{TF/AFM}}$ is the frequency of the Larmor precession (whose value is related to the applied wTF and to the internal AFM field respectively), ϕ is the initial phase of the oscillating signal (here zero), λ_{TF} , λ_{AFM} and λ_{tail}

¹The discrepancy between the present and previous studies of this compound is most likely related to a problem with the sample presented in especially Ref.¹⁶. The size of the main magnetic peak and thereby also the ordered magnetic moment is clearly smaller in Ref.¹⁶ than in our present study. We have carefully confirmed our present results using several different sample batches as well as using a multitude of μ^+ SR and NPD instruments to ensure the robustness of our current conclusions. In fact the NPD data presented in Ref.¹⁶ is most likely instead representative of a sample with significant Ca doping that suppresses the ordered Cr moment¹⁹.

are the depolarisation rates. The magnetic transition temperature can be determined by fitting the temperature dependence of the transverse field asymmetry A_{TF} to a sigmoid function. Figure 2(b) shows a plot of the wTF asymmetries as a function of temperature. Here an increase in A_{TF} is observed as across the magnetic phase transition where the system evolves from the low temperature AFM state to the PM state above T_N . The middle point of the sigmoid fitting curve provides the magnetic transition temperature $T_N = (125.99 \pm 0.08)$ K.

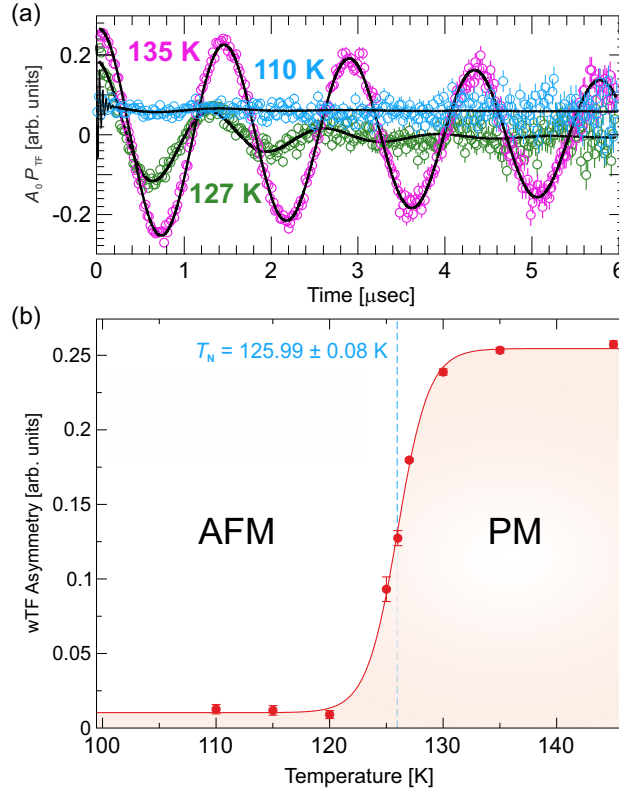


Figure 2. (a) Weak transverse field (wTF) μ^+ SR spectra in the long time domain above the transition temperature for NaCr_2O_4 . The spectra are overlapped to show the oscillation around zero asymmetry. (b) The corresponding wTF asymmetry is plotted as a function of temperature, with a fit to a sigmoid curve shown as a solid line. The transition temperature $T_N \approx 126$ K resulting from the fit is indicated by the vertical dashed line.

Inside the AFM phase (e.g., at $T = 110$ K), the low frequency associated with the wTF is completely suppressed, as clearly seen in the raw data in Fig.2 and the signal remains unchanged down to $T = 2$ K (therefore the A_{TF} temperature points below 110 K are not shown in the plot). The complete suppression of wTF asymmetry means that the entire sample volume enters the AFM phase. Above T_N , the wTF asymmetry fully recovers its maximum value, implying that the muons in the entire volume of the sample are precessing according to the weak external field. The smooth transition from full asymmetry to complete suppression of A_{TF} , without intermediate steps down to base temperature, rules out the possibility of a phase separation and/or substantial magnetic impurities.

A zero-field (ZF) μ^+ SR experiment has also been performed for different temperatures, in order to observe the evolution of the internal magnetic field distribution in NaCr_2O_4 . The muons implanted in the sample act as ultra sensitive microscopic magnetometers, which probe the internal field by following their spin polarization²¹. The resulting ZF μ^+ SR time spectra for different temperatures in the short time domain are displayed in Fig. 3(a). Here, the clear oscillations visible in the spectra are linked to the muons spins' Larmor precession, whose angular frequency (ω) changes according to the local magnetic field (of modulus B). The time dependence of the muon spin polarization can be described by exponentially relaxing oscillating functions. At base temperature $T = 2$ K the fit function chosen for NaCr_2O_4 is the following:

$$A_0 P_{ZF}(t) = \sum_{i=1,3} A_{AFi} \cos(2\pi\nu_{AFi}t + \frac{\pi\phi_{AFi}}{180}) \cdot e^{(-\lambda_{AFi}t)} + A_{\text{tail}} \cdot e^{(-\lambda_{\text{tail}}t)}. \quad (2)$$

where A_0 is the initial asymmetry of the muon decay, P_{ZF} is the muon spin polarization function. Here the distinct static

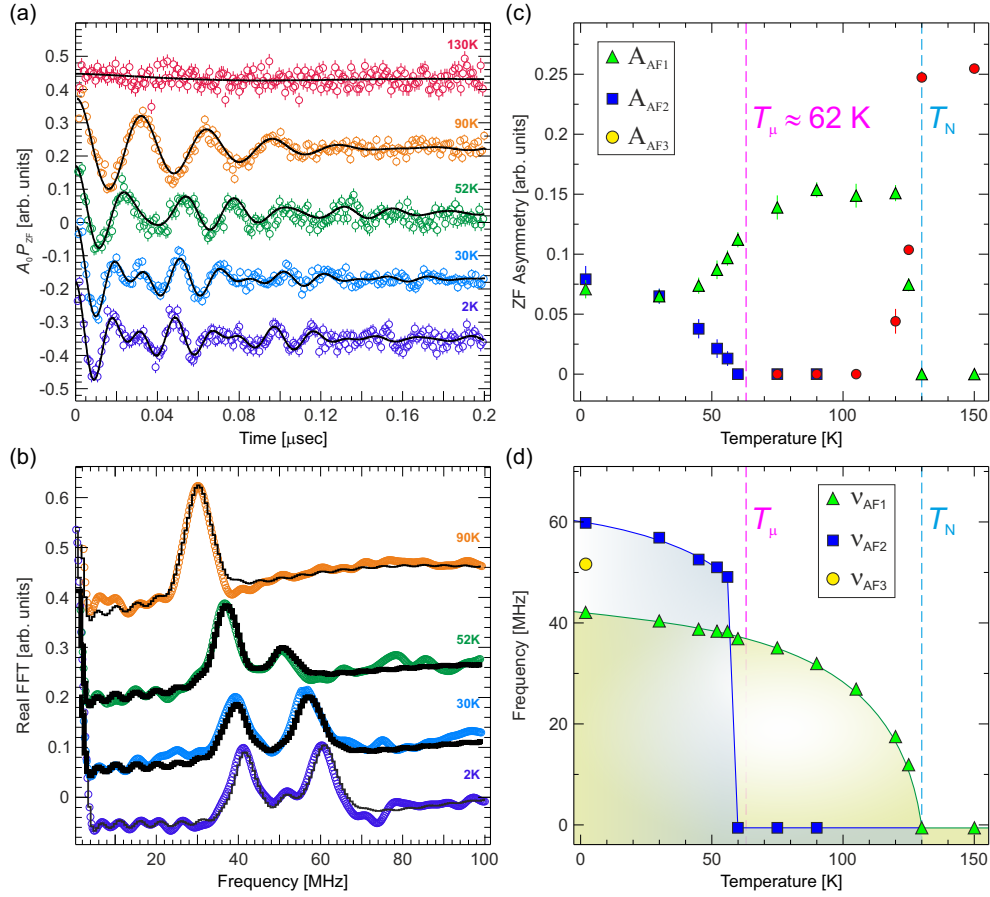


Figure 3. (a) Early time domain μ^+ SR spectra in zero field (ZF) as a function of temperature across the magnetic phase transition revealing an evolution from three to one frequency. The continuous black lines are best fits to the function shown in Eq. 2. For clarity of display, the spectra have been shifted along the y-axis. (b) Real part of the fast Fourier transform (FFT) for the NaCr_2O_4 ZF time spectra displayed in (a), with the continuous black lines again representing fits to Eq. 2. (c) Temperature dependencies of the asymmetries for the oscillating components of the ZF signal. (d) Temperature dependence of the frequencies of the muon spin Larmor precession. Vertical dashed lines indicate critical temperatures, $T_\mu \approx 62$ K and $T_N \approx 130$ K, respectively.

internal magnetic field at the muon sites, associated to the commensurate AFM ordering, results in an oscillation of the muon spin polarization (fitted with a cosine function) with three well defined frequencies for the Larmor precession: $\nu_{AF1} = (41.68 \pm 0.24)$ MHz, $\nu_{AF2} = (60.95 \pm 0.31)$ MHz and $\nu_{AF3} = (51.80 \pm 0.31)$ MHz. ϕ is the initial phase-shift of the implanted muon polarization with respect to the detectors' plane. For NaCr_2O_4 we find that $\phi \approx 0$ for all frequencies across the entire temperature range. Further, λ_{AF} is the exponential relaxation rate of the cosine function, and $A_{\text{tail}} \cdot e^{(-\lambda_{\text{tail}} t)}$ is a non oscillatory exponential tail term due to the components of the internal field that are parallel to the initial polarization direction of the muons' spins. This term is commonly found in powder samples. The presence of two clear frequencies is visible in the 2 K muon time spectra and its Fourier transform in Fig. 3(a,b). At this temperature a third frequency could also be included in the fit, however, its small amplitude (compared to the other two frequencies) makes its presence in the muon spectrum questionable. The asymmetries and frequencies of the ZF spectra as a function of temperature are displayed in Fig. 3(c,d). As the temperature increases the spontaneous oscillation of the muon spin polarization, is suppressed until only the tail component dominates the spectrum above T_N . In addition, the second frequency ν_{AF2} undergoes a full suppression for temperatures above $T_\mu \approx 62$ K [Fig. 3(d)]. Such a drastic change in the frequencies are usually related to either a structural phase transition (changing the muon stopping sites) or a change in the spin structure (e.g. spin canting). However, as we will show below in our detailed NPD study, there is no change in the atomic or magnetic structure occurring in this temperature range. Looking more carefully at the ZF asymmetries in Fig. 3(c), we see that with increasing temperature, there is a gradual shift of asymmetry from A_{AF2} to A_{AF1} . Finally, when crossing T_μ , only A_{AF1} (i.e. ν_{AF2}) survives. Most likely this means that two muon stopping sites are favorable

below T_N , but with increasing temperature the second stopping site becomes energetically unfavorable. More detailed computer modeling of the muon stopping sites in NaCr_2O_4 will be required to confirm such hypothesis.

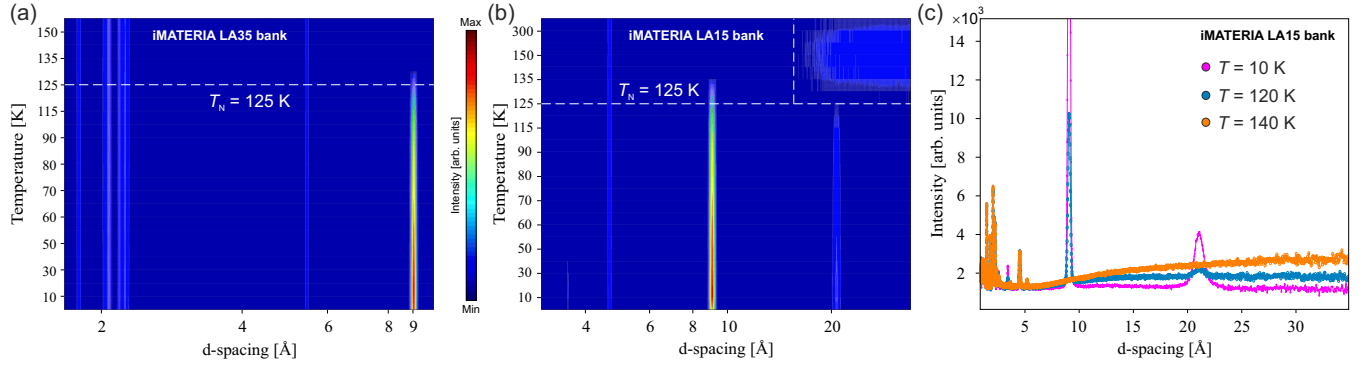


Figure 4. (a) 2D color map of the temperature dependence of the NaCr_2O_4 diffraction pattern acquired in the iMATERIA low-angle bank (LA35) shown in d -spacing. A large magnetic peak is clearly visible at $d = 9 \text{ \AA}$, and the transition temperature $T_N = 125 \text{ K}$ is shown as horizontal dashed line. (b) 2D color map of the temperature dependence of the diffraction pattern in NaCr_2O_4 acquired using the iMATERIA low(er)-angle bank (LA15) shown in d -spacing. An additional, weaker, magnetic peak is visible at $d \approx 20 \text{ \AA}$. Above T_N , a broad diffuse scattering intensity is clearly visible in the d -range surrounding such weak magnetic peak, as indicated by the dashed square region. (c) Diffraction patterns from the LA15 iMATERIA bank at different temperatures, showing the evolution of the magnetic diffuse scattering, forming the magnetic Bragg peak below T_N . Please note that the y -axes for both 2D color maps in (a) and (b) panels have non-linear temperature scales.

NPD Results

To study the temperature evolution of the magnetic structure in NaCr_2O_4 , neutron powder diffraction (NPD) patterns were collected at the time-of-flight (ToF) instrument iMATERIA in J-PARC while comparative low temperature patterns were collected also using the SPICA instrument. Figures 4(a-c) show the temperature evolution of the diffraction pattern in the high- d (low- Q) range. Here, the absence of splitting for the nuclear Bragg peaks in the low- d range, indicates that no structural transitions occur in the investigated temperature range [Fig. 4(a)]. A high-intensity magnetic peak (and several other), appearing at $T_N = 125 \text{ K}$, is clearly seen at $d = 9 \text{ \AA}$, as expected from previous characterizations. In addition, a weaker magnetic peak appears at even higher $d \sim 20 \text{ \AA}$ for $T < T_N$. These two magnetic reflections manifest a slightly different phenomenology. Indeed, in the d -range around 20 \AA , a broad diffuse scattering intensity is clearly visible above T_N [inside the dashed rectangle in Fig. 4(b)], while no such scattered intensity can be observed around $d = 9 \text{ \AA}$. The diffuse scattering indicates the presence of short-range spin correlations in the temperature range between 130 K and 300 K . Below 130 K , such disordered state is replaced by a long range magnetic order, and the diffuse scattered intensity condenses into a Bragg peak at $d \sim 20 \text{ \AA}$ [Fig. 4(c)]. The presence of high-temperature short range magnetic correlations in NaCr_2O_4 was never reported before. The behavioral difference between the strong and the weak magnetic peaks suggests that they are originated by two distinct periodic arrangements of the magnetic moments in the Cr lattice.

The magnetic and crystal structure of NaCr_2O_4 has been determined with a global procedure involving the simultaneous Rietveld refinement of diffraction patterns from all 4 ToF detector banks while keeping the cell parameters, the atomic positions and the basis vectors of the magnetic moment as common parameters. A comparative refinement for data collected in one of the low angle banks from SPICA at $T = 3 \text{ K}$ was used as additional confirmation and provided very similar results. The low temperature refined profiles with the experimental data from both instruments measured with different detector banks are displayed in Fig. 5(a-d), where the magnetic peaks are highlighted by magenta and orange arrows. The observed profiles are in very good agreement with the calculated models, as also underlined by the low values of the reliability R-factors, reported in Table 1 along with refined structural parameters at both high and low temperature.

The calculated diffraction pattern contains a nuclear and a two magnetic NaCr_2O_4 phases, plus two small impurity Cr_2O_3 and CrO_2 impurity phases. The high and low temperature nuclear phase was found to be well modeled by a orthorhombic $Pnma$ space group (No. 62), in agreement with previously reported results. In our high-resolution data we also found that the adoption of strain parameters (only relevant for the high resolution BS bank pattern) substantially improved the refinement in the full temperature range. The strain is probably a heritage of the high pressure synthesis process necessary to manufacture the sample. The Rietveld refinement of the NaCr_2O_4 magnetic phases includes the two magnetic Cr atoms in their respective crystallographic sites. The scale factors and structural parameters were constrained to be equal to their counterparts in the

Table 1. Structural lattice parameters, atomic positions and isotropic thermal displacement parameters (B_{iso}) for NaCr_2O_4 , as refined from neutron powder diffraction data (iMATERIA, global fit to all detector banks). Also shown are the refinement reliability factors for the nuclear [$R_{\text{B(nuc)}}$] and magnetic [$R_{\text{B(mag1)}}$ and $R_{\text{B(mag2)}}$] phases. All the atomic positions have the site symmetry $4c$.

	$T = 300 \text{ K}$	$T = 5 \text{ K}$
Space Group	$Pnma$	$Pnma$
a (Å)	9.01556(5)	9.0305(1)
b (Å)	2.91279(1)	2.91695(3)
c (Å)	10.41412(6)	10.3428(1)
$\alpha = \beta = \gamma$	90°	90°
Na (x, y, z)	(0.243(2), 1/4, 0.347(1))	(0.244(2), 1/4, 0.348(1))
Cr1 (x, y, z)	(0.082(1), 1/4, 0.603(1))	(0.083(2), 1/4, 0.603(1))
Cr2 (x, y, z)	(0.063(1), 1/4, 0.114(1))	(0.062(2), 1/4, 0.115(1))
O1 (x, y, z)	(0.2958(8), 1/4, 0.6489(7))	(0.297(1), 1/4, 0.6499(8))
O2 (x, y, z)	(0.3860(8), 1/4, 0.9803(7))	(0.3867(9), 1/4, 0.9805(9))
O3 (x, y, z)	(0.4768(9), 1/4, 0.2170(7))	(0.476(1), 1/4, 0.2177(9))
O4 (x, y, z)	(0.0756(9), 1/4, 0.9295(8))	(0.074(1), 1/4, 0.9287(8))
$B_{\text{iso}}(\text{Na})$ (Å ²)	0.503(5)	0.39(2)
$B_{\text{iso}}(\text{Cr1})$ (Å ²)	0.058(9)	0.025(8)
$B_{\text{iso}}(\text{Cr2})$ (Å ²)	0.093(3)	0.18(2)
$B_{\text{iso}}(\text{O1})$ (Å ²)	0.121(1)	0.09(1)
$B_{\text{iso}}(\text{O2})$ (Å ²)	0.165(1)	0.14(2)
$B_{\text{iso}}(\text{O3})$ (Å ²)	0.147(1)	0.23(1)
$B_{\text{iso}}(\text{O4})$ (Å ²)	0.207(1)	0.19(2)
$R_{\text{B(nuc)}}$ (%)	3.64	2.98
$R_{\text{B(mag1)}}$ (%)	-	0.802
$R_{\text{B(mag2)}}$ (%)	-	7.14

nuclear NaCr_2O_4 phase, for a proper estimation of the Cr moments μ_{Cr} in the two magnetic cells. The indexing of the temperature dependent magnetic Bragg reflections was achieved with the magnetic propagation vectors $k_1 = (1 \ 0 \ 1)$ and $k_2 = (0 \ 0 \ 0.497) = (0 \ 0 \ \frac{1}{2} - \delta)$, determined with the software K-Search. While the k_1 magnetic cell is commensurate (C-AFM) to the crystal structure, the k_2 cell is incommensurate (IC-AFM) and has the c -axis doubled with respect to the nuclear and k_1 magnetic cells (see also Fig. 6).

The software BasIreps provided the possible irreducible representations of the propagation vector group G_k compatible with the space group $Pnma$ and the propagation vectors k_1 and k_2 . The direct sum of 8 possible irreducible representations (IRrep) gave the reducible representation for k_1 as $\Gamma = 1\Gamma_1 \oplus 2\Gamma_2 \oplus 2\Gamma_3 \oplus 1\Gamma_4 \oplus 1\Gamma_5 \oplus 2\Gamma_6 \oplus 2\Gamma_7 \oplus 1\Gamma_8$. Among the different IRreps used to refine the magnetic phase with a trial and error approach, the Γ_7 of dimension 1 contained 2 times in Γ was selected as the one that could provide the best match. For k_2 the reducible representation can be written as $\Gamma = 1\Gamma_1 \oplus 2\Gamma_2 \oplus 1\Gamma_3 \oplus 2\Gamma_4$. Among the different IRreps used to refine the magnetic phase with a trial and error approach, the Γ_4 of dimension 1 contained 2 times in Γ was selected as the one that could provide the best match. Table 2 reports the real and imaginary basis vectors of the Γ_7 (k_1) and Γ_4 (k_2) representation for the crystallographic symmetry operators associated with the two Cr sites (Cr1 and Cr2).

The coefficients of these basis vectors for both k_1 and k_2 , namely C1 and C2, were refined as common parameters for both the Cr sites, since no significant improvement for the refinement was observed by leaving them independent. The resulting spin axial vector for k_1 has a large component along the crystallographic c -direction, a smaller component along the a -direction and zero component along the b -direction, leading to a tilt of the Cr spin with respect to the c -axis. Due to the presence of imaginary basis vectors for the IRrep of k_2 , the resulting spin axial vector has a cycloidal-like modulation along the a -axis, reminiscent of the magnetic structure found in the isostructural compound NaMn_2O_4 ⁶. The latter material also exhibits two distinct C-AFM and IC-AFM magnetic cells. However, while in NaMn_2O_4 the AFM coupling and the IC modulation of the Mn moments develop along the zigzag Mn chains, in NaCr_2O_4 the magnetic structures develop along the rutile chains in

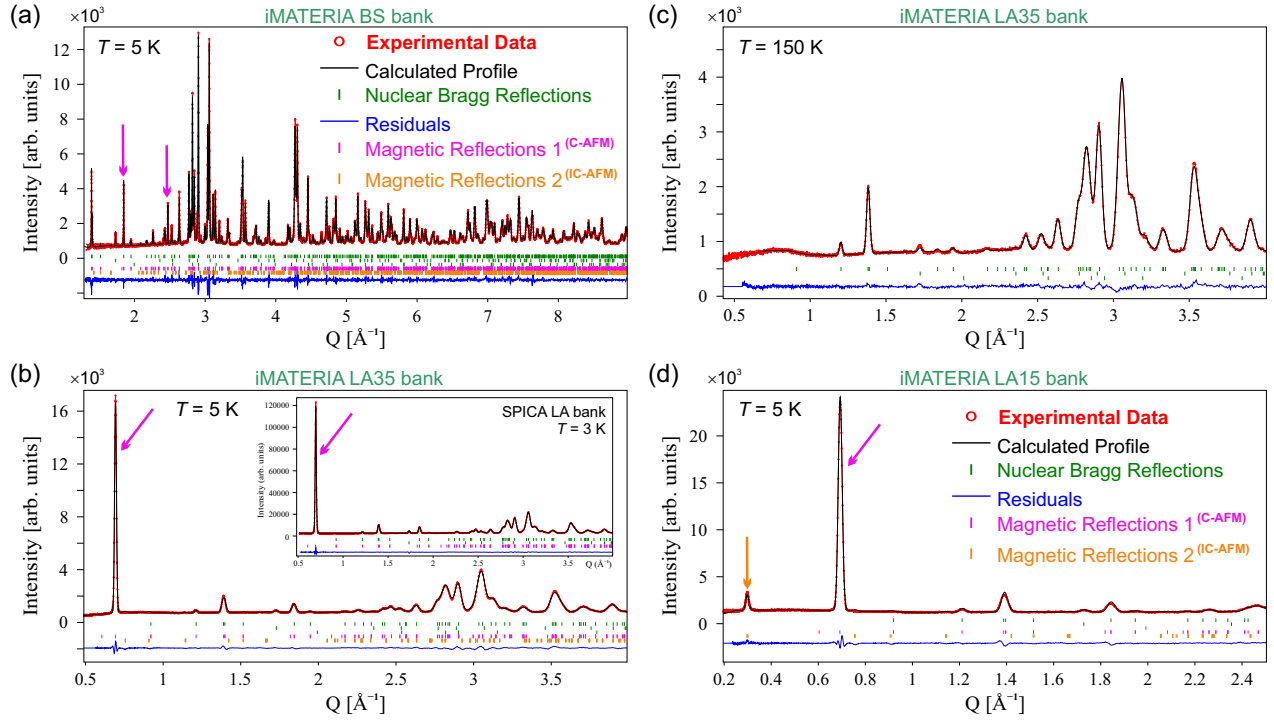


Figure 5. Neutron diffraction pattern of NaCr_2O_4 acquired from the (a) the backscattering (BS) and (b) 35° (LA35) low-angle banks of iMATERIA at base temperature. The inset in (b) shows the diffraction pattern of NaCr_2O_4 from the low-angle LA bank of SPICA at base temperature (for comparison). (c) Neutron diffraction pattern from the 35° (LA35) bank of iMATERIA, above the transition temperature (no magnetic peaks). (d) Neutron diffraction pattern from the 15° (LA15) bank of iMATERIA, at base temperature. The arrows indicate the magnetic Bragg peaks in the diffraction patterns, where magenta and orange colors refer to the commensurate (C-AFM) and incommensurate (IC-AFM) magnetic propagation vectors, respectively.

the ac -plane. As a result, the C-AFM alignment of the Cr spins exhibits canting, and the IC cycloidal Cr spin arrangement display systematic suppression of the Cr moment on the spin inversion sites. A graphic representation of the obtained magnetic structures is displayed in Fig. 6(a-c). For the k_1 cell, the canted AFM coupled FM double rutile chain along the c -axis, are clearly visible in Fig. 6(a), while the FM zig-zag chains running along the b -axis are emphasized in Fig. 6(b). For the k_2 cell, the modulated cycloidal arrangement of the Cr moments along the a -axis is displayed in Fig. 6(c). Figure 6(d) explicitly shows the different Cr and O sites in the lattice, including the oxygen site (O1) that mediates the AFM coupling between the zig-zag Cr chains.

For the k_1 structure, the canting angle $\theta_c = (8.8 \pm 0.5)^\circ$, estimated from the average value of the components of the basis vector C1 and C2 through the temperature range from base-T to 100K. This angle is estimated with higher confidence with respect to the one estimated previously¹⁶. The total moment of the Cr atoms, calculated as the modulus of the Cr spin axial vector averaging among the low temperature fluctuations, is $\mu_{\text{Cr}}^{\text{C}} = (4.30 \pm 0.01)\mu_{\text{B}}$ for the k_1 structure, and $\mu_{\text{Cr}}^{\text{IC}} = (2.20 \pm 0.03)\mu_{\text{B}}$ for the k_2 structure.

Discussion

The $\mu_{\text{Cr}}^{\text{C}}$ value found in this work is remarkably higher than the expected spin only value for a system with a nominal valence state $\text{Cr}^{3.5+}$, since $S_{\text{Cr}^{3+}} = 3.87\mu_{\text{B}}$ and $S_{\text{Cr}^{4+}} = 2.83\mu_{\text{B}}$ (which are actually consistent with $\mu_{\text{Cr}}^{\text{IC}}$). Values closer to the measured $\mu_{\text{Cr}}^{\text{C}}$ value could be achieved by including the orbital contributions to the total Cr moment, which would sum up to an ordered moment of 5.2 and $4.5\mu_{\text{B}}$ for Cr^{3+} and Cr^{4+} , respectively. However, orbital contributions from Cr in an octahedral environment is expected to give negligible contribution to the total moment. This is due to orbital quenching in a crystal field²², making this option less probable. Indeed, even though orbital contributions of vanadium in octahedral environment was in fact recently suggested in VI_3 by $\mu^+\text{SR}$ and XAS^{23,24}, for NaCr_2O_4 , an unusual mixed valence electronic state has instead been reported⁸. It was suggested that Na substitution in the solid solution $\text{Na}_x\text{Ca}_{1-x}\text{Cr}_2\text{O}_4$ does not result in electrons removed from the Cr site, as expected in typical mixed valence compounds. Here, the electrons are instead removed from the O sites, to relax charge

Table 2. Basis vectors of the irreducible representations $\Gamma_7 (k_1)$ and $\Gamma_4 (k_2)$ of the magnetic propagation vector group G_k .

$\Gamma_7 (k_1)$: C-AFM		
SYMM	x,y,z	
BsV ₁ (Re)	(1 0 0)	(0 0 1)
BsV ₁ (Im)	(0 0 0)	(0 0 0)
SYMM	-x+1/2,-y,z+1/2	
BsV ₂ (Re)	(1 0 0)	(0 0 -1)
BsV ₂ (Im)	(0 0 0)	(0 0 0)
SYMM	-x,y+1/2,-z	
BsV ₃ (Re)	(1 0 0)	(0 0 1)
BsV ₃ (Im)	(0 0 0)	(0 0 0)
SYMM	x+1/2,-y+1/2,-z+1/2	
BsV ₄ (Re)	(1 0 0)	(0 0 -1)
BsV ₄ (Im)	(0 0 0)	(0 0 0)
$\Gamma_4 (k_2)$: IC-AFM		
SYMM	x,y,z	
BsV ₁ (Re)	(1 0 0)	(0 0 1)
BsV ₁ (Im)	(0 0 0)	(0 0 0)
SYMM	-x+1/2,-y,z+1/2	
BsV ₂ (Re)	(-0.022 0 0)	(0 0 0.022)
BsV ₂ (Im)	(-1 0 0)	(0 0 1)

frustration and realize a negative charge transfer state⁸. In fact, the large value of the Cr moment (μ_{Cr}^C) measured in this work could be explained by the negative charge transfer state induced in $NaCr_2O_4$, since it could lead to a Cr valence Cr^{2+} in a high spin state $d^3 (t_{2g}^3 e_g^1)$. The expected spin only value for Cr^{2+} is $4.9 \mu_B$, which is comparable to μ_{Cr}^C . Therefore, our results could indirectly confirms the unusual charge transfer present in $NaCr_2O_4$ ⁸. While it was not commented on, since CO is not observed in this system^{10,14}, this kind of electronic configuration also suggest highly fluctuating vacancies. A similar situation was also observed for the 1D mixed valance system $K_2Cr_8O_{16}$ ²⁵, which is structurally analogous to $NaCr_2O_4$.

Additionally, our result is consistent with the predictions of recently published DFT calculations²⁰, which envision a spin disproportionation between the Cr1 and Cr2 sites. This would lead to the existence of high-spin Cr sites in the magnetic ground state of $NaCr_2O_4$. The authors of Ref.²⁰ evaluated the modulus of the Cr moment as $\approx 2\mu_B$ for both low and high spin states, which is close to the value found in Ref.¹⁶. Nevertheless, they also acknowledge that, due to the uncertainty of the results of Ref.¹⁶, their estimation cannot be experimentally validated. The large value of μ_{Cr}^C obtained in this work is also consistent with a magnetic coupling mechanism mediated by ligand holes in $NaCr_2O_4$, as also suggested in references^{8,11}. This aspect will be further expanded below in the discussion related to the coupling mechanism involved in the magnetic order.

The temperature dependence of the structure factor $F[0\ 0\ -1]$, obtained as the square root of the integrated intensity of the of the large k_1 magnetic peak (0 0 -1) and smaller k_2 magnetic peak (0 0 0), are plotted in Fig. 7(a). The solid lines are fits to the power law:

$$f(x) \propto (1 - \frac{x}{T_c})^\beta. \quad (3)$$

The temperature evolution of the diffraction peak is related to the order parameter of the magnetic phase transition. By fitting it with Eq. 3 it is possible to estimate the onset of the magnetic transition temperature, and acquire some indications about the type of symmetry breaking that the system undergoes. The onset of the magnetic transition was found at $T = (130 \pm 0.003)$ K, in good agreement with the μ^+ SR measurements. The value of the critical exponent, estimated for the k_1 peak, was found $\beta_1 = 0.245 \pm 0.007 \approx \frac{1}{4}$, suggesting that the AFM-PM phase transition in $NaCr_2O_4$ is located at a tricritical point²⁶. Within the Landau mean-field approximation, this means that the onset of the magnetic transition in $NaCr_2O_4$ is a point between the edge of a second order transition and the ordinary critical point of a first-order transition^{27,28}. The tricritical behavior observed in this work, together with the dramatic increase in the magnetization with the relatively small externally applied field of 3.5 T (associated to a spin-flop transition)⁹, are compatible with the fact that a possible hidden metamagnetic state²⁹ is established in this material at the edge of the AFM-PM transition. This conjecture is based on the qualitative agreement between $NaCr_2O_4$ and

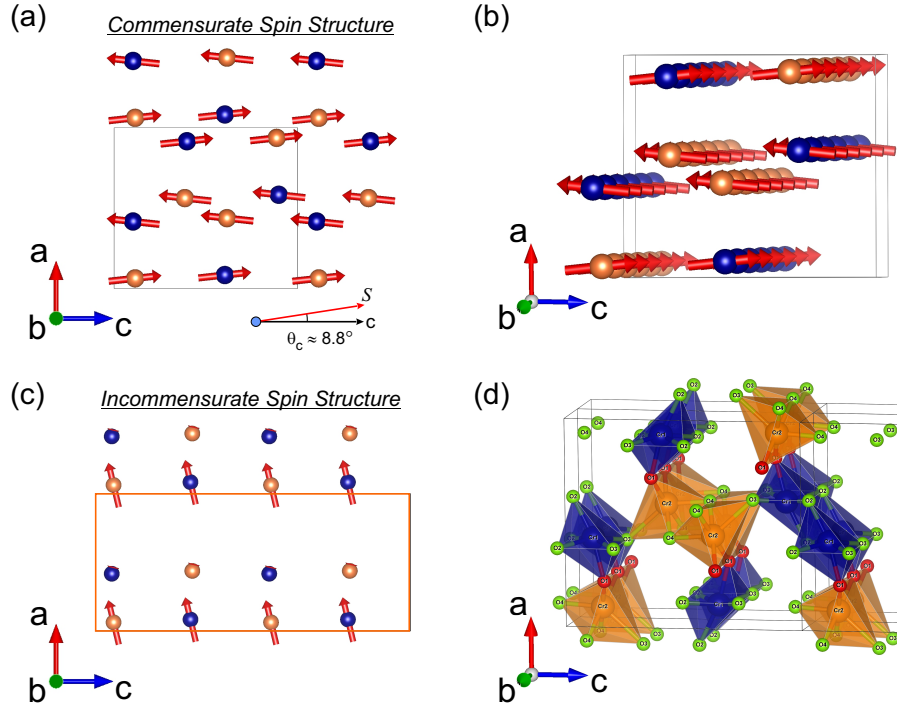


Figure 6. (a,b) Commensurate (C-AFM) spin structure of NaCr₂O₄ with $k_1 = (1\ 0\ 1)$ at $T = 5\text{ K}$. The Na atoms have been removed for clarity of display. The spin canting [$\theta_c \approx (8.8 \pm 0.5)^\circ$] and the AFM coupling of the chains along the a -axis is visible from the ac -plane orientation. The ferromagnetic alignment of the Cr spin within the chains along the b -axis is emphasized in the (b) panel. (c) Incommensurate (IC-AFM) magnetic supercell with $k_2 = (0\ 0\ \sim 1/2)$. The spin alignment in this case is cycloidal, but a systematic suppression of the anti-parallel Cr moments along the a -axis also occurs. (d) CrO₆ octahedra with the oxygen sites explicitly labelled. The oxygen site (O1) that mediates the AFM coupling between the zig-zag Cr chains is highlighted in red.

tricritical metamagnetic systems that manifest a similar phenomenology, i.e., NiCl₂, 2H₂O, Ni(NO₃)₂^{30–32}. In these systems, magnetic field dependent changes in magnetization and susceptibility were erroneously identified as spin-flop transitions. Nevertheless, studies of the evolution of the magnetic structure under high magnetic fields would be necessary to resolve the ambiguity of the field induced transitions, and to outline of the magnetic phase diagram of NaCr₂O₄. The temperature dependencies of both the coefficients of the k_1 basis vectors C1, C2 follow the same trend as the structure factor F[0 0 -1] [cf. Fig. 7(a,b)], suggesting that the canting angle of the Cr spin axial vector is maintained across the full temperature range, as its modulus decreases. The temperature trend for the structure factor F[0 0 0] of the k_2 magnetic peak is also displayed in Fig. 7(a). Here the critical exponent is estimated as $\beta_2 = 0.31 \pm 0.01$, which is close to the value for a 3D Heisenberg AFM with a 1-dimensional order parameter²⁶, suggesting a more conventional magnetic ground state for this phase.

The temperature dependence of the unit cell parameters are displayed in Fig. 7(c,d). On cooling, the value of the a -axis decreases monotonically down to $T \approx 60\text{ K}$, where an inversion of trend is observed. Phenomenologically, such inversion coincides with the suppression of the second muon frequency at $T_\mu \approx 62\text{ K}$. This could be a weak indication that the subtle changes in the lattice could yield an energetically unfavorable situation for one of the muon stopping sites. The value of the b -axis instead increases monotonically, with a trend similar to the one observed for the evolution of the magnetic parameters in Fig. 7(a,b), with a clear change in slope at the magnetic transition temperature $T_N = 125\text{ K}$. The c -axis undergoes a monotonic decrease down to base temperature, with a similar but mirrored behavior as the one observed in the b -axis. The temperature evolution of the unit cell parameters shows evidence of coupling between the crystal and magnetic structure. However, since the magnetic ordering does not induce a structural transition towards a different lattice symmetry, but only very slight changes in the lattice parameters, such coupling does not seem to be very strong. Finally, the μ^+ SR precession signal displayed a gradual transition from two to one frequency at $T_\mu \approx 62\text{ K}$ [Fig. 3(b)]. As already mentioned above, since no dramatic effect is present in the NPD patterns (neither nuclear nor magnetic) around these temperatures (Fig. 7), the reason for the change in the frequency spectrum is probably due to a change in the structural muon sites. Here the temperature evolution of the lattice and atomic positions could simply result in that one of the muon stopping site becomes energetically unfavorable above T_μ .

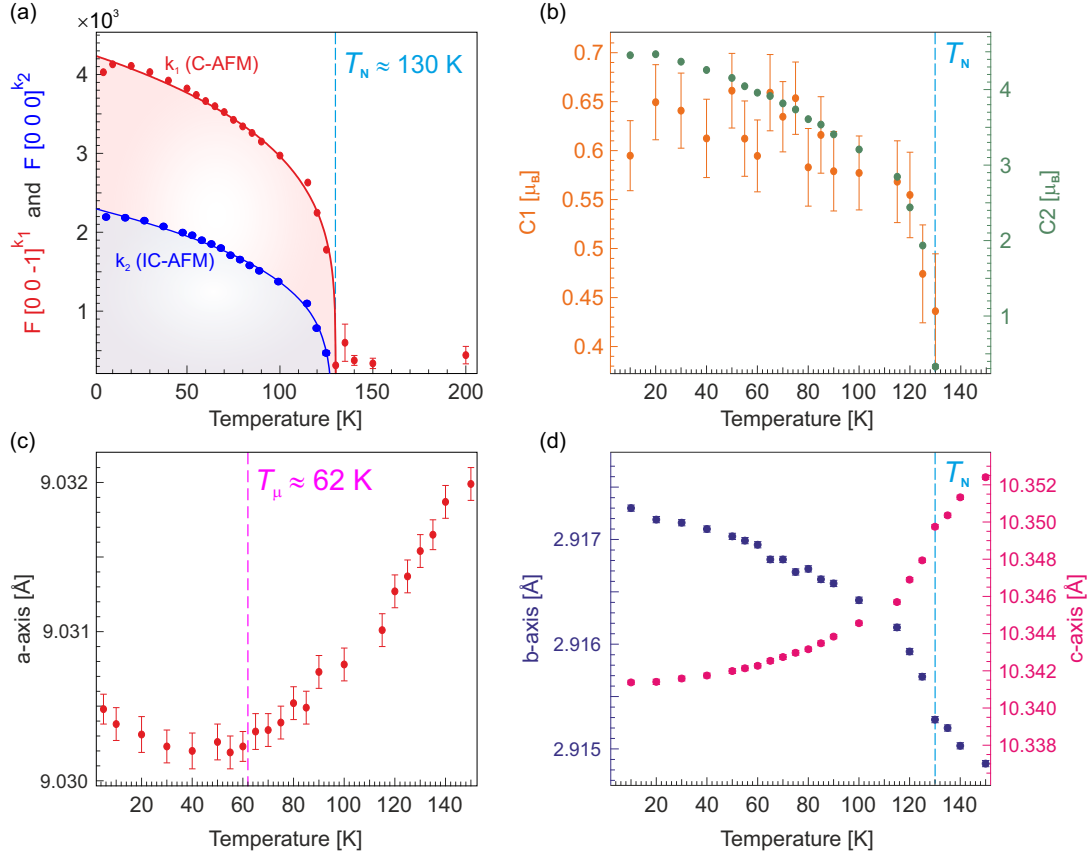


Figure 7. (a) Structure factor (F) of the large k_1 magnetic peak (0 0 -1) as well as the weaker k_2 magnetic peak (0 0 0) with fits to Eq. 3 shown as a solid line. (b) Temperature dependence of the coefficients of the k_1 basis vectors, $C1$ and $C2$. (c-d) Temperature dependence of the unit cell parameters. The magnetic transition temperature (T_N) along with the anomaly related to changes in the number of muon frequencies (T_μ , see also Fig. 3) are shown as vertical dashed lines.

It appears that, depending on the reciprocal orientation of the octahedra, FM and AFM exchange interaction are established between the Cr ions. In particular, for the k_1 magnetic structure, three different magnetic couplings seem to be in place below T_N : ① An inter-chain FM exchange mechanism is always established across the edge sharing octahedra in the Cr1 and Cr2 chains. ② An intra-chain FM exchange mechanism is always established across the corner sharing octahedra between the chains stacked along the c -direction (through the oxygen atom in the crystallographic site O3). ③ an intra-chain AFM coupling is always established across corner sharing octahedra between the chains stacked along the a direction (through the oxygen atom in the crystallographic site O1). Consistently with the large value of the Cr moment extracted in this work, we can consider the ligand holes concentrated at the corner oxygen O1 and O3 sites¹⁰ as the main responsible for the occurrence of the C-AFM phase k_1 . Using the arguments similar to the ones presented in reference³³, the FM inter-chain coupling can be indeed interpreted in terms of a double exchange FM mechanism mediated by the hopping of the O3 ligand holes. This would involve Cr orbitals with one localized electron per site and one with itinerant character, through the bond $Cr1 - \widehat{O3} - Cr2$. In fact, the O ions on the edges shared by the octahedra in the zig-zag double chain (O2, O4), were found to give insignificant contributions to the bands near the Fermi level¹⁰. Therefore, the observed inter-chain FM coupling can be considered a consequence of the intra-chain FM double exchange. This is compatible with the temperature evolution of the crystal structure, in which a monotonic increase of the b -axis on cooling suggests an increase of the Cr-Cr distances within the zig-zag double chain (i.e., compatible with a Coulomb repulsion effect). A similar phenomenology was observed in other systems such as $K_2Cr_8O_{16}$ and CrO_2 ^{2,33-35}.

Despite the dominance of FM double-exchange interaction, intra-chain AFM coupling is established along the c -axis double rutile chains. It has been suggested that the AFM coupling is due to a weak super-exchange coupling through the bond $Cr1 - \widehat{O1} - Cr2$ ¹⁶. However, it can naively be argued that an AFM super-exchange interaction across a $Cr - \widehat{Anion} - Cr$ bond requires a bond angle of 180° ³⁶. Cases in which the AFM super-exchange mechanism occurs across bond angles that deviate

from 180° can of course be realized in the presence of complex crystal-field symmetries of the magnetic ions (like in our case, with the distorted octahedral coordination of Cr ions). However, in NaCr_2O_4 the value of the bond angle $\text{Cr1} - \text{O1} - \text{Cr2} = 125.58(5)^\circ$, is very far from 180° (is actually closer to 90° , which would favor FM coupling not AFM). Therefore we suggest the mutual hopping of 2 itinerant electrons between the two Cr sites, aided by the O1 ligand holes, as a possible alternative mechanism to explain the intra-chain AFM coupling in NaCr_2O_4 . The hopping of correlated itinerant electrons was suggested as the possible mechanisms to explain the magnetic ordering in CrO_2 ³³. Such suggestion was though discarded since it would have lead to AFM ordering, which is not observed in CrO_2 . Since the $\text{Cr1} - \text{O1} - \text{Cr2}$ and $\text{Cr1} - \text{O3} - \text{Cr2}$ bonds are structurally equivalent and the O1 and O3 sites are both preferred for the localization of the ligand holes, a similar hopping coupling mechanism would be expected. The only difference between the two bonds would be the mutual orientation of the electronic orbitals in the non-equivalent Cr sites. Here, the different distortions between Cr1O_6 and the Cr2O_6 octahedra, remove the degeneracy of the Cr-3d orbitals, leading to one localized and two itinerant orbitals for the Cr1 site, and two localized and one itinerant orbital for the Cr2 site¹⁰. Due to the lack of inversion symmetry between Cr ions, the canting of the moments in this spin configuration is consistent with an anisotropic AFM exchange including an antisymmetric Dzyaloshinsky-Moriya (DM) exchange term^{37,38}.

The proposed correlated electron hopping mechanism for the AFM coupling is deduced as a logic consequence of these observations. In this regard, given the discrepancy between the moduli of the ordered moments of the two C-AFM and IC-AFM structures (i.e. $\mu_{\text{Cr}}^{\text{C}} = 4.3 \mu_{\text{B}}$ vs. $\mu_{\text{Cr}}^{\text{IC}} = 2.2 \mu_{\text{B}}$), and the different values of their critical exponents $\beta_1 \sim \frac{1}{4}$ and $\beta_2 \sim 0.31$, we suggest that the itinerant hopping electrons are responsible for the k_1 long-range C-AFM order, while the localized electrons are responsible for the IC-AFM order. To verify this conjecture, neutron diffraction studies under applied magnetic fields would be an optimal and direct test. Indeed, magnetic structures with itinerant character are sensitive to external magnetic fields, while the localized ones are not³⁹.

To summarize, the detailed and partly revised magnetic structure of NaCr_2O_4 is presented in this work. The analysis of high-resolution data shed new light on this interesting compound. In addition to a canted C-AFM phase with propagation vector $k_1 = (1\ 0\ 1)$, an additional IC cycloidal-like magnetic phase is identified with propagation vector $k_2 = (0\ 0\ \frac{1}{2} - \delta)$. Following the temperature evolution of the structure factor of the magnetic reflections, indications of unconventional critical behavior for the k_1 magnetic phase transition in NaCr_2O_4 were found. In particular, we suggest that the magnetic transition might be at the edge of a tricritical point with possible formation of a metamagnetic hidden phase. Weak interplay between the crystal and magnetic structure, evidenced by the comparison between the μ^+ SR and NPD data, is compatible with the absence of geometric frustration. The value of the ordered Cr moments of the C-AFM and IC-AFM structures were extracted as $\mu_{\text{Cr}}^{\text{C}} = 4.3 \mu_{\text{B}}$ and $\mu_{\text{Cr}}^{\text{IC}} = 2.2 \mu_{\text{B}}$, respectively. The high $\mu_{\text{Cr}}^{\text{C}}$ value is consistent with a double exchange coupling mechanism mediated by itinerant Cr moments (i.e., the ligand-hole hopping mechanism), for the k_1 C-AFM order. On the other hand, the lower $\mu_{\text{Cr}}^{\text{IC}}$ value is consistent with a coupling mechanism mediated by exchange interactions between localized Cr spins, for the k_2 IC order. The value of the canting angle of the Cr spin axial vector for the C-AFM structure has been determined with high accuracy as $\theta_c = (8.8 \pm 0.5)^\circ$. A FM double-exchange interaction, together with an AFM correlated itinerant electrons hopping interaction, have been proposed as the mechanisms driving the magnetically ordered k_1 phase in NaCr_2O_4 . Magnetic field dependent studies of the magnetic structure would be relevant to discern the effects of the localized and itinerant electrons on the ordered moments, and clarify the magnetic (H/T) phase diagram of the NaCr_2O_4 compound.

Methods

Polycrystalline samples of NaCr_2O_4 were prepared from a stoichiometric mixture of NaCrO_2 , Cr_2O_3 , and CrO_3 at 1300°C under a pressure of 7 GPa. The samples were synthesized at the National Institute for Material Science (NIMS) in Tsukuba, Japan. The samples were preliminary characterized using in-house x-ray diffraction (XRD). This showed that all sample batches were single phase, with a CaFe_2O_4 -type *Pnma* structure. Further details on the sample preparation can be found in Ref.¹¹.

The μ^+ SR spectra have been acquired, as a function of temperature, at the multi purpose surface muon instrument Dolly⁴⁰, at the Paul Scherrer Institute (PSI) in Switzerland⁴¹. Approximately 500 mg of powder sample was packed in a $1 \times 1 \text{ cm}^2$ area envelope made from Aluminum-coated Mylar tape (0.05 mm thickness). The envelope was attached to a low background Cu sample holder inserted in a helium exchange gas cryostat (temperature range: 1.6 K to 300 K).

The neutron powder diffraction (NPD) measurements were performed at the time of flight powder diffractometers iMATERIA⁴² and SPICA⁴³ at the high intensity proton accelerator facility J-PARC, in Japan. The powder samples ($m \approx 0.72 \text{ g}$) were mounted into cylindrical vanadium cells with diameters 6 mm (for SPICA) and 5 mm (for iMATERIA). The cells were sealed using an aluminium cap, aluminium screws and indium wire. The cell was mounted on a closed cycle refrigerator to reach temperatures between 2 K and 300 K. SPICA and iMATERIA are designed to reach a wide range in reciprocal space, while measuring at a single scattering angle by means of large position sensitive detectors. Different detector banks provide different d-ranges (Q-ranges) with gradually changing resolutions, in particular in SPICA the high angle detector bank, provides d-range from 0.3 Å up to 3.7 Å with a resolution $\Delta d/d = 0.12\%$, while the low angle (LA) detector bank has a d-range from 0.5 Å

up to 11 Å. In iMATERIA the backward detector bank (BS), allows a d-range from 0.181 Å up to 5.09 Å with a resolution $\Delta d/d = 0.16\%$, while the low angle detector banks (LA35 and LA15) allow to resolve d-ranges from 0.25 Å up to 40 Å. These features make the high angle banks very suitable for detailed structural characterization while the low angle banks are ideal to unequivocally identify any magnetic Bragg peak, which usually appear in the high-d (low-Q) range.

The crystal and magnetic structure determination was carried out with the FullProf software suite⁴⁴. All images involving crystal structure were made with the VESTA software⁴⁵, the parameter fitting has been performed with the software Igorpro⁴⁶ and the μ^+ SR data were fitted using the *musrfit*⁴⁷ software package.

References

1. Adler, D. Mechanisms for metal-nonmetal transitions in transition-metal oxides and sulfides. *Rev. Mod. Phys.* **40**, 714 (1968).
2. Toriyama, T. *et al.* Peierls mechanism of the metal-insulator transition in ferromagnetic hollandite K₂Cr₈O₁₆. *Phys. Rev. Lett.* **107**, 266402 (2011).
3. E. Nocerino *et al.* Unconventional Superconductivity in the Spinel Thin Film LiTi₂O₄ Investigated by Low-Energy μ^+ SR, *Unpublished* (2022).
4. Bednorz, J. G. & Müller, K. A. Possible highT_c superconductivity in the Ba-La-Cu-O system. *Zeitschrift für Physik B Condens. Matter* **64**, 189–193 (1986).
5. Urushibara, A. *et al.* Insulator-metal transition and giant magnetoresistance in La_{1-x}Sr_xMnO₃. *Phys. Rev. B* **51**, 14103 (1995).
6. Matsubara, N. *et al.* Neutron powder diffraction study of NaMn₂O₄ and Li_{0.92}Mn₂O₄: Insights on spin-charge-orbital ordering. *Phys. Rev. Res.* **2**, 043143 (2020).
7. Nozaki, H. *et al.* Incommensurate spin-density-wave order in quasi-one-dimensional metallic antiferromagnet NaV₂O₄. *Phys. Rev. B* **81**, 100410 (2010).
8. Taguchi, M. *et al.* Unusual coexistence of negative and positive charge transfer in mixed-valence Na_xCa_{1-x}Cr₂O₄. *Phys. Rev. B* **96**, 245113 (2017).
9. Sakurai, H. *et al.* Unconventional colossal magnetoresistance in sodium chromium oxide with a mixed-valence state. *Angewandte Chemie Int. Ed.* **51**, 6653–6656 (2012).
10. Toriyama, T., Konishi, T. & Ohta, Y. Electronic structure of calcium-ferrite-type Cr oxide NaCr₂O₄. In *Proceedings of the International Conference on Strongly Correlated Electron Systems (SCES2013)*, 017003 (2014).
11. H. Sakurai. Magnetic and electronic properties of Ca(1-x)Na_xCr₂O₄ double-exchange interactions and ligand holes. *Phys. Rev. B* **89**, 024416 (2014).
12. Tokura, Y. *Colossal magnetoresistive oxides* (CRC Press, 2000).
13. Furukawa, N. Temperature dependence of conductivity in (La, Sr) MnO₃. *J. Phys. Soc. Jpn.* **64**, 3164–3167 (1995).
14. Takeda, H., Shimizu, Y., Itoh, M., Sakurai, H. & Takayama-Muromachi, E. Magnetic frustration effects in the new colossal magnetoresistance oxide NaCr₂O₄. *J. Korean Phys. Soc.* **62**, 1914–1918 (2013).
15. Damay, F. *et al.* Zigzag ladders with staggered magnetic chirality in the s = 3/2 compound β -NaCr₂O₄. *Phys. Rev. B* **81**, 214405 (2010).
16. Nozaki, H. *et al.* Magnetic structure for NaCr₂O₄ analyzed by neutron diffraction and muon spin-rotation. *Phys. B: Condens. Matter* (2017).
17. Nozaki, H. *et al.* Internal magnetic field in the zigzag-chain family (Na, Ca) Cr₂O₄. In *Journal of Physics: Conference Series*, vol. 551, 012013 (IOP Publishing, 2014).
18. Sugiyama, J. *et al.* Magnetic ground state of novel zigzag chain compounds, NaCr₂O₄ and Ca_{1-x}Na_xCr₂O₄, determined with muons and neutrons. *Phys. Procedia* **75**, 868–875 (2015).
19. E. Nocerino *et al.* *Unpublished* (2022).
20. Yamaoka, H. *et al.* Electronic and crystal structures of (Na_{1-x}Ca_x) Cr₂O₄ with anomalous colossal magnetoresistance. *Phys. Rev. B* **102**, 235150 (2020).
21. Blundell, S. Spin-polarized muons in condensed matter physics. *Contemp. Phys.* **40**, 175–192 (1999).

22. Datta, S. XLIX. Studies in paramagnetism.—I. on the mechanism of quenching of orbital magnetic moment in paramagnetic ions of the iron group. *The London, Edinburgh, Dublin Philos. Mag. J. Sci.* **17**, 585–602 (1934).
23. Forslund, O. K. *et al.* Refined magnetic structure of VI_3 . *arXiv preprint arXiv:2210.17455* (2022).
24. De Vita, A. *et al.* Influence of orbital character on the ground state electronic properties in the van der waals transition metal iodides VI_3 and CrI_3 . *Nano letters* **22**, 7034–7041 (2022).
25. Bhohe, P. A. *et al.* Electronic structure evolution across the peierls metal-insulator transition in a correlated ferromagnet. *Phys. Rev. X* **5**, 041004 (2015).
26. Yaouanc, A. & De Reotier, P. D. *Muon spin rotation, relaxation, and resonance: applications to condensed matter*. 147 (Oxford University Press, 2011).
27. Huang, K. *Statistical mechanics* (John Wiley & Sons, 2008).
28. Griffiths, R. B. Thermodynamics near the two-fluid critical mixing point in $\text{He}_3\text{-He}_4$. *Phys. Rev. Lett.* **24**, 715 (1970).
29. Stryjewski, E. & Giordano, N. Metamagnetism. *Adv. Phys.* **26**, 487–650 (1977).
30. Swüste, C., Botterman, A., Millenaar, J. & De Jonge, W. The magnetic phase diagram and exchange parameters in $\text{NiCl}_2 \cdot 2\text{H}_2\text{O}$. *J. Chem. Phys.* **66**, 5021–5030 (1977).
31. Schmidt, V. & Friedberg, S. Metamagnetism of $\text{Ni}(\text{NO}_3)_2 \cdot 2\text{H}_2\text{O}$. *Phys. Rev. B* **1**, 2250 (1970).
32. Polgar, L. & Friedberg, S. Low-temperature heat capacity of the metamagnet $\text{Ni}(\text{NO}_3)_2 \cdot 2\text{H}_2\text{O}$. *Phys. Rev. B* **4**, 3110 (1971).
33. Korotin, M., Anisimov, V., Khomskii, D. & Sawatzky, G. CrO_2 : A self-doped double exchange ferromagnet. *Phys. Rev. Lett.* **80**, 4305 (1998).
34. Forslund, O. K. *et al.* Neutron scattering on a ferromagnetic metal-insulator transition compound $\text{K}_2\text{Cr}_8\text{O}_{16}$ (2021).
35. Schlottmann, P. Double-exchange mechanism for CrO_2 . *Phys. Rev. B* **67**, 174419 (2003).
36. Kanamori, J. Superexchange interaction and symmetry properties of electron orbitals. *J. Phys. Chem. Solids* **10**, 87–98 (1959).
37. Dzyaloshinsky, I. A thermodynamic theory of “weak” ferromagnetism of antiferromagnetics. *J. physics chemistry solids* **4**, 241–255 (1958).
38. Moriya, T. Anisotropic superexchange interaction and weak ferromagnetism. *Phys. review* **120**, 91 (1960).
39. Li, H.-F. *et al.* Distinct itinerant spin-density waves and local-moment antiferromagnetism in an intermetallic ErPd_2Si_2 single crystal. *Sci. reports* **5**, 1–7 (2015).
40. (2017). www.psi.ch/smus/InstrumentDollyEN.
41. (2017). [/www.psi.ch](http://www.psi.ch).
42. Ishigaki, T. *et al.* IBARAKI materials design diffractometer (iMATERIA)—versatile neutron diffractometer at J-PARC. *Nucl. Instruments Methods Phys. Res. Sect. A: Accel. Spectrometers, Detect. Assoc. Equip.* **600**, 189–191 (2009).
43. Yonemura, M. *et al.* Development of SPICA, new dedicated neutron powder diffractometer for battery studies. In *Journal of Physics: Conference Series*, vol. 502, 012053 (IOP Publishing, 2014).
44. Rodríguez-Carvajal, J. Recent advances in magnetic structure determination by neutron powder diffraction. *Phys. B: Condens. Matter* **192**, 55–69 (1993).
45. Momma, K. & Izumi, F. VESTA: a three-dimensional visualization system for electronic and structural analysis. *J. Appl. Crystallogr.* **41**, 653–658 (2008).
46. WaveMetrics. IGOR Pro, scientific data analysis software.
47. A. Suter and B. M. Wojek. Musrfit: A free platform-independent framework for μSR data analysis. *Phys. Proc.* **30**, 69, DOI: [10.1016/j.phpro.2012.04.042](https://doi.org/10.1016/j.phpro.2012.04.042) (2012).

Acknowledgements (not compulsory)

The $\mu^+\text{SR}$ measurements were performed at instrument *Dolly* of the Swiss Muon Source ($S\mu\text{S}$), at the Paul Scherrer Institute in Villigen, Switzerland. The NPD measurements were performed at the instruments iMATERIA and SPICA of the neutron spallation source J-PARC (beamtime proposals: 2019A0330, 2019B0420). The authors wish to thank the staff of PSI and J-PARC for their great support during the $\mu^+\text{SR}$ and NPD experiments. This research is funded by the Swedish Foundation for

Strategic Research (SSF) within the Swedish national graduate school in neutron scattering (SwedNess), as well as the Swedish Research Council VR (Dnr. 2021-06157 and Dnr. 2017-05078), and the Carl Tryggers Foundation for Scientific Research (CTS-18:272). J.S. is supported by the Japan Society for the Promotion Science (JSPS) KAKENHI Grant No. JP18H01863 and JP20K21149. Y.S. and O.K.F. are funded by the Chalmers Area of Advance - Materials Science.

Author contributions statement

E.N., J.S., and M.M. conceived the experiments. E.N., O.K.F., N.M., F.M., D.A., J-C.O., T.S, I.U., Y.S., J.S. and M.M. conducted the experiments. E.N, O.K.F., J.S., N.M., and M.M. analyzed the results. The samples were synthesized by H.S., who also conducted the initial sample characterizations. E.N. and M.M made all the figures. E.N. created the first draft, and all co-authors reviewed and revised the manuscript.

Data availability statement

All the data of this work are available from the corresponding authors on request.

Competing interests

The authors declare no competing interests.

The corresponding author is responsible for submitting a [competing interests statement](#) on behalf of all authors of the paper.